Journal of Environmental Chemical Engineering 11 (2023) 110921

Contents lists available at ScienceDirect

Journal of Environmental Chemical Engineering

journal homepage: www.elsevier.com/locate/jece

Pt-Ni contact engineering in carbon nitride based photocatalysts for hydrogen production

Rocío Sayago-Carro [a], Pablo Piqueras-Pérez [a], Ruifeng Du [b], Junshan Li [c], Jing Yu [b,d], Jordi Arbiol [d,e], Anna Kubacka [a], Andreu Cabot [b,e,*], Marcos Fernández-García [a,**]

[a] Instituto de Catálisis y Petroleoquímica, CSIC. C/Marie Curie 2, 28049 Madrid, Spain
[b] Catalonia Institute for Energy Research - IREC, Sant Adrià de Besòs, Barcelona 08930, Catalonia, Spain
[c] Institute for Advanced Study, Chengdu University, 610106 Chengdu, China
[d] Catalan Institute of Nanoscience and Nanotechnology (ICN2), CSIC, BIST, Campus UAB, Bellaterra, 08193 Catalonia, Spain
[e] ICREA, Pg. Lluís Companys 23, 08010 Barcelona, Catalonia, Spain

ARTICLE INFO

Editor: Javier Marugan

Keywords:
Photocatalysis
Quantum efficiency
Hydrogen
Pt-Ni alloy
Carbon nitride
Nanosheet, Methanol

ABSTRACT

The effect of a binary PtNi co-catalyst supported on graphitic carbon nitride nanosheets is studied in the photo-production of hydrogen from methanol:water mixtures. The physicochemical analysis provides evidence that the carbon nitride support allows the formation of highly dispersed PtNi nanoparticles with an average composition of Pt 85 % Ni 15 %. The binary system outperforms the monometallic Pt and Ni counterparts and renders an extraordinary quantum efficiency of 8.8 % for hydrogen photo-production. The formation of a PtNi alloy, with a Pt-enriched surface and electronic properties influenced by the heterometallic contact, provides high and stable activity, mostly as a consequence of the effects that the co-catalyst exerts on the charge carrier handling capability of the solid.

1. Introduction

Environmental concerns and particularly global warming demand an urgent energy transition from fossil fuel derivatives to greener energy sources and technologies. Among potential new energy carriers, hydrogen appears as a firm candidate to diminish the environmental impact and reach carbon neutrality. Hydrogen plays also a central role in the chemical industry to produce a significant number of building block molecules such as ammonia as well as many other commodities such as plastics. While hydrogen is mainly produced through methane dry reforming, a positive environmental impact can only be achieved when using zero carbon or net zero carbon processes and precursors such as biomass [1]. In all such processes, catalysis plays a key role [2,3].

The production of hydrogen through photocatalysis uses light as the only energy source. It has advantages over the classic thermal process as it frequently uses mild reaction conditions, e.g. room temperature and pressure. Yet, a typical bottleneck for the application of this technology is the relatively low quantum efficiency (QE) of the process. This low QE can have multiple sources, being those related to charge handling and surface phenomena the most relevant ones. Among the charge handling aspects, key parameters are the photogeneration of charge carriers through light absorption, the control of charge carrier de-excitation and the transport of charge to the relevant surface sites. In terms of surface phenomena, key parameters are the surface adsorption, activation, and evolution of the reactants [2,4,5].

Among photocatalytic materials, carbon nitride is a rather successful alternative semiconductor to the well-known titania. Beyond its excellent intrinsic properties, carbon nitrides can be produced in a wide range of architectures with nanometer regime features that can be tuned to optimize photocatalytic performance [6–9]. The adjustment of the nanostructural parameters should take into consideration the surface area and its direct chemical effects on reagent adsorption and activation. Additionally, light-related effects concerning charge carrier handling, and particularly the control of charge recombination, need to be considered to promote activity under light excitation. An especially convenient architecture is that of nanosheets offering large surface areas for cocatalyst dispersion and adsorption of reactants while at the same time enabling an effective transport of charge carriers. In the case of

* Correspondng author at: Instituto de Catálisis y Petroleoquímica, CSIC. C/Marie Curie 2, 28049 Madrid, Spain.
** Correspondng author.
E-mail addresses: acabot@irec.cat (A. Cabot), mfg@icp.csic.es (M. Fernández-García).

https://doi.org/10.1016/j.jece.2023.110921
Received 29 May 2023; Received in revised form 30 August 2023; Accepted 31 August 2023
Available online 2 September 2023

carbon nitride, the nanosheet morphology appears as a direct consequence of its laminar structure, although materials with high surface area require specific preparation methods [6–9].

The photocatalytic production of renewable hydrogen from biomolecules such as alcohols usually requires the use of composite catalysts that include a co-catalyst dispersed on the surface of a semiconductor support. The chemical nature of the co-catalyst as well as their interaction with the support are key aspects to be controlled to ensure high activity. Typically, noble metals and, particularly, platinum, are used to boost activity [6,10,11]. Yet more complex formulations of the co-catalyst such as binary alloys are commonly tested in the quest of maximizing activity [12–15]. In the case of platinum, materials having Pt in intimate contact and alloyed with noble and non-noble metals have been tested for the photocatalytic production of hydrogen [16,17]. The case of platinum modification by adding non-noble nickel has been studied. However, details of the Pt-Ni interaction have not been fully unveiled mainly as a cause of the nanometric size of the catalytic particles. Moreover, the resulting systems have been frequently tested using non-renewable chemicals (e.g. triethanolamine, TEOA) and were found to be unstable over a long time on stream tests [18,19].

Here we will detail the synthesis of PtNi nanoparticles supported on graphitic C_3N_4 (g-CN). We demonstrate the close interaction between the two metals, as well as a large dispersion of the binary nanoparticles on the high surface area g-CN nanosheets, can render a highly active and stable system for the photocatalytic production of hydrogen from a renewable source such as methanol in a water medium. Moreover, based on a rigorous analysis of the quantum efficiency, we will show that the system is among the top-performing catalyst ever reported in terms of quantum efficiency.

2. Experimental section

2.1. Catalysts preparation

2.1.1. Layered g-C_3N_4 (g-CN)

Layered g-CN was prepared through a two-step thermal polymerization of urea. A covered crucible with 10 g of urea was heated to 550 °C at a rate of 2 °C min^{-1} for 4 h under air. The resulting powder was ground with the mortar. This material was subsequently placed in a covered crucible and heated to 520 °C at a rate of 5 °C min^{-1} for 2 h under air.

2.1.2. Pt/g-CN

A photoreduction method was utilized to load on the prepared layered carbon nitride support. To this end, 100 mg of g-CN were dispersed in 100 mL solution containing 10 mL methanol and 400 μL of a 25.625 mmol/L $HPtCl_6$ aqueous solution (for 1 wt% Pt). The solution obtained was treated using N_2 for 30 min to ensure an anaerobic state and illuminated for 30 min with UV light (300 W Xe lamp). The obtained composite was collected by centrifuging, washed with ethanol and water 2 times, and was finally dried at 60 °C for 12 h ($Pt_{1\ \%}$/g-CN).

2.1.3. Ni/g-CN and PtNi/g-CN

100 mg of g-CN were added into 100 mL deionized water containing 10 mL triethanolamine, 4.3 g nickel acetate tetrahydrate (for 1 wt% Ni), and 500 mg sodium hypophosphite. After 30 min sonication, argon was flowed through the solution for 30 min. Subsequently, the solution was subjected to UV–vis illumination (300 W Xe lamp) under continuous stirring under argon for 30 min. The resulting powder was collected and washed 3 times (using water and ethanol consecutively) and dried under vacuum for 6 h ($Ni_{1\ \%}$/g-CN). The $Ni_{0.5\ \%}Pt_{0.5\ \%}$/g-CN sample was prepared through the same method but adding 0.5 wt% Ni and 0.5 wt% Pt.

2.2. Catalysts characterization

The atomic composition of the catalysts was measured using atomic emission coupled with inductively coupled plasma atomic emission spectroscopy (ICP-AES; Optima 3300DV Perkin Elmer spectrometer, USA). X-ray diffraction (XRD) patterns were obtained using a Bruker D8 Advance diffractometer with Ni-filtered Cu-Kα radiation (λ = 1.5406 Å). Applying the Williamson–Hall method, primary particle size information was obtained for the diffracting phases [20]. The morphology of the samples was determined using a scanning electron microscope (SEM) from Carl Zeiss (Auriga). High-resolution transmission electron microscopy (HRTEM) images and scanning transmission electron microscopy (STEM) studies were carried out on an FEI Tecnai F20 field emission gun microscope operated at 200 kV. For samples degassed overnight at 140 ℃, a Micromeritics Tristar-II 3020 equipment (USA) was utilized to carry out nitrogen physisorption experiments and measure textural properties. UV−vis diffuse-reflectance experiments were acquired on a Varian Cary300 apparatus (USA). UV–visible spectra were displayed with the help of the Kubelka-Munk transformation [21]. Band gap analysis of carbon nitride containing samples was carried out plotting $(h\nu a)^{1/2}$ ($h\nu$ = excitation energy, a = absorption coefficient, proportional to the Kubelka-Munk transform) as a function of the incoming light energy. This procedure considers the carbon-based material an indirect gap semiconductor [22]. Photoluminescence spectra were acquired at room temperature with the help of a Fluorescence Spectrophotometer (Horiba FluoroMax Plus, Germany). Samples were excited at 380 nm. XPS data were recorded using a SPECS® spectrometer (UK) with a PHOIBOS® 150 WAL hemispherical energy analyzer with angular resolution (< 0.5∘). The equipment has an XR 50 X-Ray Al-Xray and μ-FOCUS 500 X-ray monochromator (Al excitation line) source. The binding energies (BE) were referenced to the C 1s peak using a 284.6 eV energy. Fitting procedures were carried out with the CASA 2.3.25 program using a Shirley background [23].

2.3. Activity measurements

A liquid phase reactor containing a suspension of the catalyst (1 g L^{-1}) in a methanol:water liquid was used to generate hydrogen gas. The gas is continuously eliminated from the reaction and reached the detection system (Omnistar 200 mass spectrometer) with the help of an argon stream. UV-near visible (280–420 nm) illumination was obtained from a Xe 500 W arc lamp with the help of dichroic and IR filters from Quantum LOT. As measured using actinometry, the impinging photon flux at the reactor is ca. 1.1×10^{-8} Einstein cm^{-3} s^{-1}. The semi-continuous gas-liquid reactor characteristics, optimization of operating conditions, as well as the light intensity measurements and calculations are reported elsewhere [24,25].

Values for activity parameters, e.g. the reaction rate and quantum efficiency, were obtained following IUPAC rules [26]. As shown in Eq. (1), the quantum efficiency can be obtained as the ratio between the reaction rate (r) and the rate of photon absorption (e^a). Both parameters correspond to average values over the entire volume of the reactor (denoted with A suffix)

$$QE(\%) = \frac{\langle r \rangle_A}{\langle e^a \rangle_A} \times 100 \tag{1}$$

The e^a observable was in turn calculated through the analysis of the light intensity over the reactor following Eq. (2), as suggested by the IUPAC.

$$\frac{dI_{\lambda,\underline{\Omega}}(\underline{x})}{ds} = -\kappa_\lambda I_{\lambda,\underline{\Omega}}\left(\underline{x}\right) - \sigma_\lambda I_{\lambda,\underline{\Omega}}\left(\underline{x}\right) + \frac{\sigma_\lambda}{4\pi}\int_{\underline{\Omega}'=4\pi} p\left(\underline{\Omega}' \rightarrow \underline{\Omega}\right) I_{\lambda,\underline{\Omega}'} \quad d\underline{\Omega}' \tag{2}$$

As an initial step, optical measurements of the suspended catalysts were used to solve Eq. (2). The optical measurements render the spectral absorption (κ_λ) and the spectral scattering (σ_λ) coefficients. Together

with the scattering phase ($p\left(\underline{\Omega}'\rightarrow\underline{\Omega}\right)$, calculated using the Henyey-Greenstein equation, they are used to solve the Radiative Transfer Equation (RTE) in our reactor (Eq. (2)).[27] In this work, Eq. (2) is solved using the discrete ordinate method, allowing to obtain the intensity of light throughout the reactor volume ($I_{\lambda,\underline{\Omega}}\left(\underline{x}\right)$) and, finally, of the e^a parameter, $e^a = \int_\lambda \kappa_\lambda(\underline{x}) \bullet \int_{\Omega=4\pi} I_{\lambda,\underline{\Omega}}\left(\underline{x}\right) d\Omega d\lambda$. A detailed description of all experimental and numerical methods summarized in this section are described in previous works [24,25].

3. Results and discussion

3.1. Physicochemical characterization

Fig. 1 displays SEM micrographs of the produced materials, including g-CN, Ni/g-CN, PtNi/g-CN, and Pt/g-CN. The g-CN support shows a sheet-like structure allowing a large dispersion of metal nanoparticles (brighter spots). The chemical nature and the particle size distribution of metal particles are discussed below with the help of other techniques. We just mention that SEM images show aggregates of metal particles composed by several single crystallites with an average particle size in the range of a few nanometers, as would be determined below from the XRD patterns. Fig. 2 A displays the nitrogen adsorption–desorption isotherms and pore size distribution obtained for the PtNi/g-CN sample. In all cases, our samples exhibit type IV isotherms with H3 hysteresis loops, indicating the presence of a dominant mesoporous structure. As shown in the inset of Fig. 2A, negligible contribution of microporosity (well below 1 %) as well a significant contribution from macropores (size above 50 nm) can be also observed. In fact, the analysis of the porosity (Table S1) indicates that mesoporosity/macroporosity account for ca. 55–60/45–40 % of the pore size distribution of the fresh samples. The PtNi/g-CN presents a dual pore size with mesopores with relatively low size (ca. 2.5–4 nm) and meso and macropores having higher sizes (maximum at ca. 38 nm; see inset of Fig. 2 A). As previously noted in the literature, this can be rationalized by considering pores along the nanosheets and between them.[2,4,5] The BET area of the bare mesoporous support reach a value of ca. 80 $m^2\ g^{-1}$ and decreases to 50–60 $m^2\ g^{-1}$ when the metals are included in the catalyst formulation (Table 1). The decrease in the BET surface area obtained when introducing the metals indicates that the metals partially alter the pores of the support. In presence of the co-catalysts and irrespective of their chemical nature, analysis of the porosity shows changes mostly associated with the pores of the dual distribution with size in the tends of nanometers (Table 1; Table S1), suggesting that the metal component is mainly altering the staking of carbon nitride nanosheets. Owing to the two-step process used for the production of the g-CN-supported metal nanoparticles involving the initial production of the g-CN and the posterior use of this support to grow the metal using a photoreduction procedure, relatively mild differences are encountered between the metal-containing catalysts and the bare support in terms of morphological properties (Table 1). Note on the other hand, the rather similar morphological properties displayed by all the metal-containing samples.

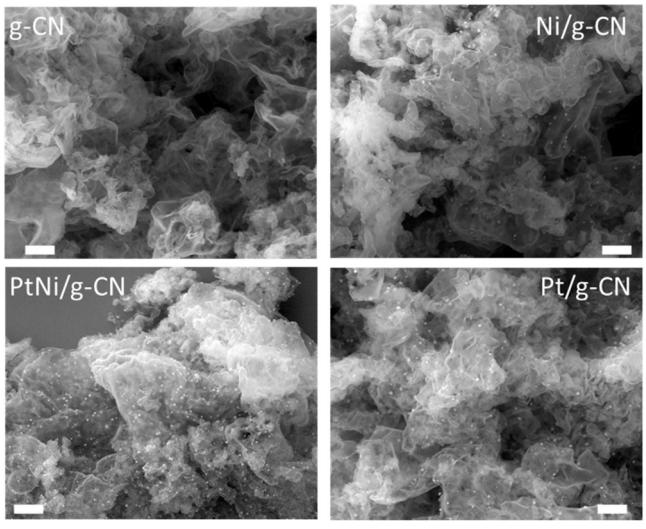

Fig. 1. SEM images of the g-CN, Ni/g-CN, PtNi/g-CN and Pt/g-CN catalysts as labeled in each panel. Scale bar = 1 μm.

The presence of the graphitic-type carbon nitride and the structural stability of such support after metal impregnation can be inferred from the infrared results presented in Fig. 2B. The most significant band to test the structural similarity between the samples is the one located at ca. 823 cm^{-1}, assigned to the breathing mode of the tris-z-triazine in the graphitic type structure [6,28,29]. A modest effect of the co-catalyst presence can be noted. The IR spectra also display the bands associated with the stretching modes of the CN heterocycles (1200–1600 cm^{-1}) as well as N-H and O-H moieties above ca. 3000 cm^{-1}. As expected for high surface area materials, the catalysts are particularly enriched in N-H terminal moieties, as can be deduced from the presence of the peaks at ca. 3090 and 3190 cm^{-1} [6,28]. Considering these contributions, no significant differences are visible between the samples of the series.

The XRD profiles of the samples are shown in Fig. 2 (panel C). As expected from the analysis of IR results, the diffraction patterns are dominated by a g-CN peak corresponding to the interlayer-stacking, (002) reflection at ca. 27.5 degrees [6,28]. To complete the analysis of the g-CN, UV–visible spectroscopy was used (Fig. 2D). A strong absorption decrease was observed in the limit between the UV and visible regions (below ca. 400–420 nm). Taking into account the indirect semiconductor nature of g-CN, the analysis of the spectra renders a band gap energy value close to 2.8 eV for all samples (Figure S1 and Table 2), which is consistent with the reported values for g-CN.[6–8] No significant differences between samples were encountered considering the band gap energy (Table 2). Thus, aside the BET surface area and pore distribution changes, no significant effect is observed in the graphitic carbon nitride support by the inclusion of the co-catalyst(s) in the powders.

The catalysts contained a total of 1 wt% of the metal in all cases (error below 3.9 %) according to chemical analysis (ICP-AES) results. Yet, the presence of the co-catalysts can be observed in the XRD patterns. This is due to the low (X-ray) absorption cross-section of the carbon nitride component (Fig. 2C). In addition to the above-mentioned peaks related to the graphitic carbon nitride support, peaks easily ascribable to metallic face-centered cubic (FCC) structures can be observed for all the samples containing metals [30]. The dominant (111) peak, located between ca. 39.9 and 44.2 degrees in our samples, can be easily spot out by comparison with the corresponding metal reference patterns included in Fig. 2C. For the PtNi/g-CN sample an average crystallite size of ca. 5 nm can be obtained through the analysis of the XRD patterns. Note also that the bimetallic PtNi/g-CN sample displays the (111) FCC peak at an intermediate position between the monometallic samples, although certainly closer to the Pt/g-CN. Analysis of the XRD profile indicates that the cell parameter decreases from the Pt monometallic reference by ca. 2.5 %. As Pt-based alloys follow the Vergard law, [31–33] this datum indicates that the PtNi bimetallic particles have an average composition close to ca. 15 at % of Ni and 85 % of Pt, i.e. are Pt-rich. Considering the metal content measured with chemical analysis, the low quantity of Ni present in the metallic particles implies the existence of additional nickel-containing phases. This is below analyzed with the help of microscopy and XPS techniques.

To confirm the presence and analyze the structural characteristics of the metal nanoparticles we carried out combined HRTEM and XPS analyses. The microscopy analysis of the samples is illustrated in Fig. 3, S2,

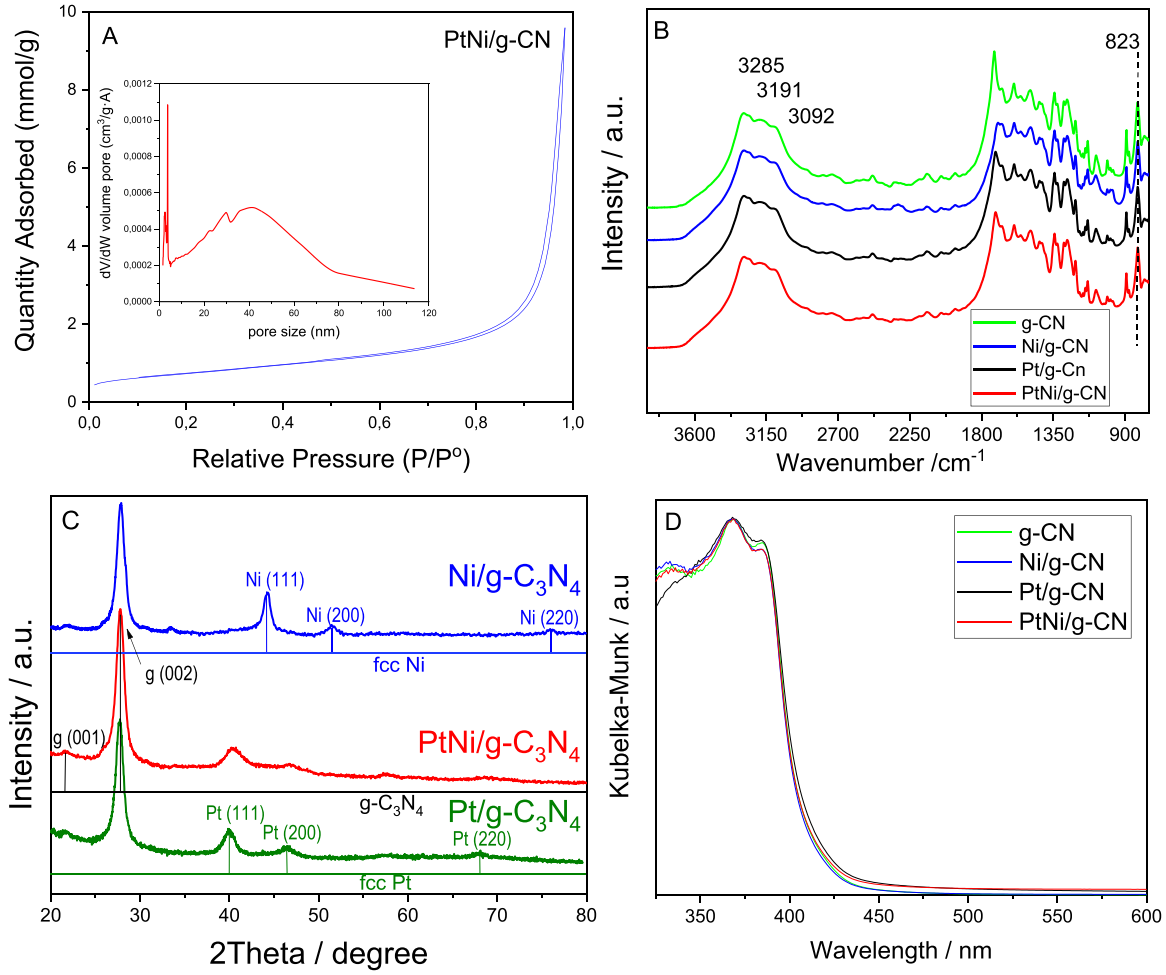

Fig. 2. (A) Nitrogen adsorption-desorption isotherm and pore distribution of the PtNi/g-CN sample. (B) IR spectra for the samples. Vertical dashed lines are included at the metal FCC (111) peak maximum. (C) XRD patterns for the samples. Reference patterns; g-C3N4 JCPDS 87-1526; Ni JCPDS 04-0850 Pt JCPDS 04-0802. (D) UV–visible spectra for the samples.

Table 1
Textural properties of the catalysts including BET area of pre / post-reaction samples.

Sample	BET area (m^2g^{-1})	Pore volume (cm^3g^{-1})	Pore size (nm)
g-CN	87.4/80.1	0.56/0.51	30.0/30.4
Ni/g-CN	58.7/54.1	0.32/0.31	23.0/23.0
Pt/g-CN	56.9/52.9	0.33/0.30	23.3/23.5
PtNi/g-CN	58.7/52.1	0.34/0.32	24.2/24.5

Table 2
Band gap energy (eV) values for the samples.

Sample	Pre-reaction	Post-reaction
g-CN	2.80	2.77
Ni/g-CN	2.79	2.81
Pt/g-CN	2.81	2.79
PtNi/g-CN	2.83	2.80

and S3, presenting results for the Pt/g-CN (Fig. 3 and S2) and PtNi/g-CN (Fig. 3 and S3) samples. The porous nanosheet-type morphology of the graphic carbon nitride is illustrated in the dark-filed images presented in Fig. 3A,C. The HRTEM micrographs and the corresponding electron diffraction patterns presented in Fig. 3B,D, S2 and S3 show that some metal crystals are aggregated but single crystallytes have sizes in the range 2–8 nm. For the Pt/g-CN sample, the metal structure can be assigned to the cubic Pt (space group = Fm-3m) with a=b=c= 3.92 Å. For the crystalline domain presented in Fig. 3B, the Pt lattice fringe distances were measured to be 0.202 nm, 0.139 nm and 0.196 nm, at 45.18° and 90.11° which could be interpreted as the cubic Pt phase, visualized along its [010] zone axis. From the crystalline domain presented in Fig. 3D, the NiPt lattice fringe distances were measured to be 0.225 nm, 0.192 nm and 0.223 nm, at 48.10° and 112.78°, which could be interpreted as the cubic NiPt phase, visualized along its [011] zone axis. The analysis of the single particle reveals a cubic NiPt (space group = Fm-3 m) with a=b=c= 3.76 Å. We highlight the significant decrease detected in the cell parameter of the Pt FCC crystallites when introducing Ni to form PtNi. The crystallite cell parameter measured with microscopy is associated with a bimetallic PtNi particle significantly more enriched in Ni (ca. 32 % vs. 15 %) than the average composition obtained from the XRD analysis. This indicates that the Pt-Ni contact in the metal nanoparticles takes place within a relatively broad range of alloy composition, although they are all Pt-rich entities according to the Vergard's law [31–34]. An extended HRTEM analysis of the PtNi/g-CN sample, considering multiple particles, showed a significant dispersion in lattice parameters, which is consistent with a related dispersion in compositions. The relatively broad range of chemical compositions observed in bimetallic particles with size in the range of a few nanometers has been previously reported and is a characteristic feature of nanostructured alloys supported in high surface area materials [35,36]. Nevertheless, within each particle, we observed a homogeneous distribution of Pt and Ni as displayed in Fig. 3E which shows electron energy

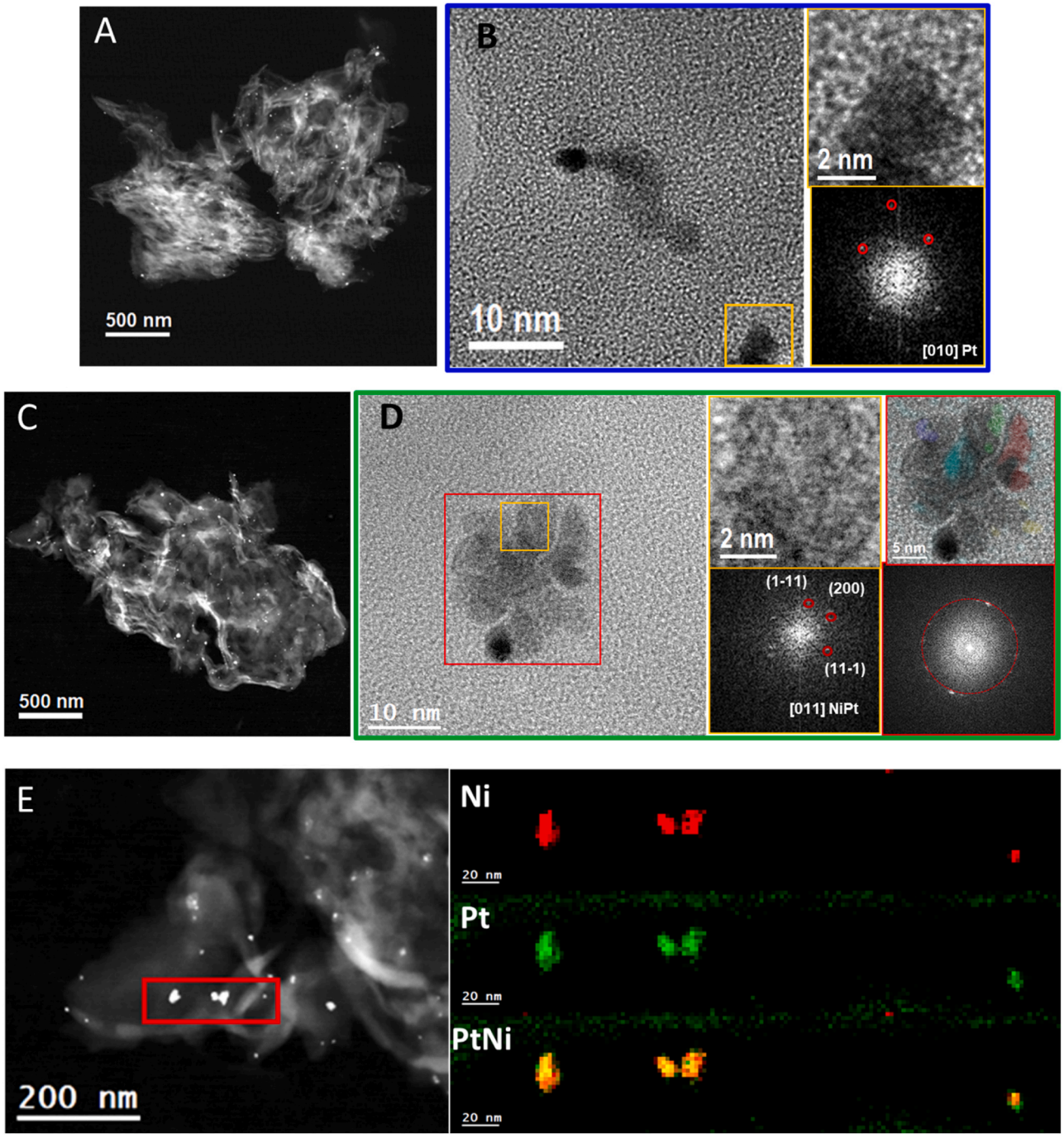

Fig. 3. Electron microscopy analysis of the Pt/g-CN (A,B) and PtNi/g-CN (C,D) samples. (A) HAADF-STEM image of Pt/g-CN. (B) HRTEM micrograph of Pt/g-CN, detail of the metal particle inside the orange box and corresponding electron diffraction pattern. (C) HAADF-STEM image of PtNi/g-CN. (D) HRTEM micrograph of PtNi/g-CN, detail of the metal crystal inside the orange box and of the whole aggregate within the red box, and corresponding electron diffraction patterns. (E) HAADF-STEM image of PtNi/g-CN and EELS chemical composition maps obtained from the red squared area. Ni $L_{2,3}$ at 855 eV (red), Pt $M_{4,5}$-edge at 2122 eV (green).

loss spectroscopy (EELS) elemental composition maps of some PtNi particles obtained from the red squared region in the HAADF-STEM micrograph (left). It should be noted that to obtain a proper EELS signal, the analyzed particles were the largest observed, which were significantly bigger than the value of the average size, being this nearly 5 nm according to diffraction.

To further investigate the metal nanoparticles, the Pt 4f and Ni 2p XPS spectra were recorded. Fig. 4 summarizes the XPS results for the PtNi/g-CN sample. Figures S4 and S5 display data for the Ni/g-CN and Pt/g-CN samples, respectively. In the PtNi/g-CN sample, the Ni 2p XPs signal shows a characteristic shape attributable to Ni^{2+} species, showing the typical main peak and shake-up satellite structure. The Ni $2p_{3/2}$ contribution peaks at 855.8 eV (Fig. 4A) [37]. Note that the absence of a metallic (zero valent) Ni contribution in the PtNi/g-CN (Ni 2p) XPS signal is a direct consequence of the average chemical composition of the alloy particles. Assuming that Pt is completely alloyed (e.g. absence of a single zero-valent Pt phase, as suggested by the XRD and microscopy studies), only ca. 5 % of the Ni present in the powder would be involved in the $Pd_{0.85}Ni_{0.15}$ alloy phase. Thus, the majority of Ni should render an XPS signal rather similar to the one of the monometallic Ni/g-CN sample (see Fig. 4A and Figure S4). Differences between the PtNi/g-CN and Pt/g-CN references are however encountered when studying the Pt

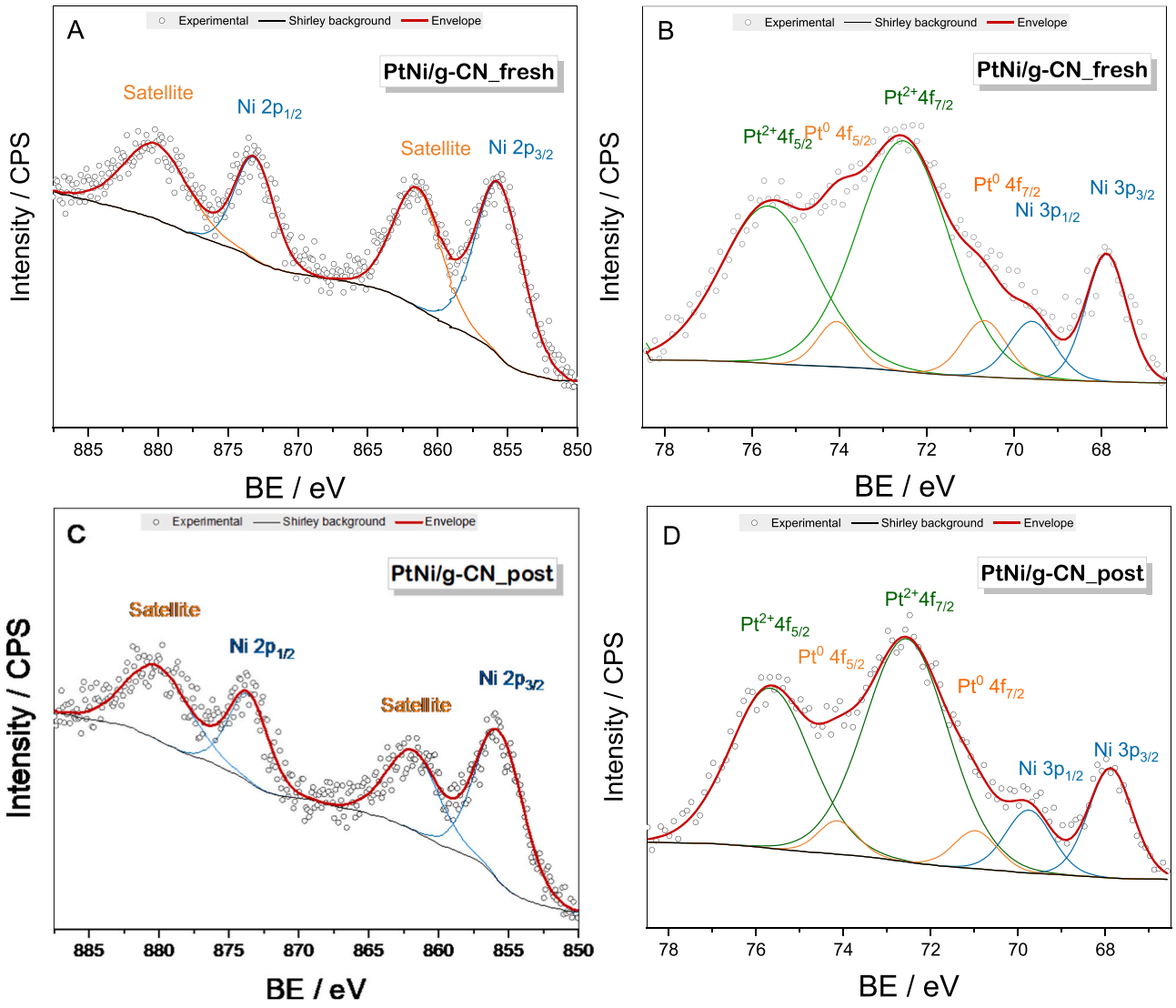

Fig. 4. (A,C) Ni 2p and (B,D) Pt 4f+Ni3p XPS spectra and fitting results for the PtNi/g-CN sample before (labeled fresh) and after (labeled post) reaction.

counterpart. Considering first the monometallic Pt/g-CN sample, the Pt $4f_{7/2}$ XPS peak is detected at ca. 70.1 eV (Figure S5). This is characteristic of nanometric Pt particles having the metallic state, as reported previously [24,25,38]. A drastic difference in Pt oxidation state is however observed in the corresponding Pt $4f_{7/2}$ XPS peak of the PtNi/g-CN sample with respect to the monometallic Pt counterpart (Fig. 4B vs. Figure S5). To analyze the mentioned Pt 4f region, we note that the Ni 3p contribution is relatively close and has to be considered to analyze the Pt $4f_{7/2}$ XPS peak [37,39]. The Ni 3p peaks are visible in Fig. 4B. The Ni $3p_{3/2}$ peak is located at ca. 67.9 eV. Note that, as expected from the results of the Ni 2p XPS study, this corresponds to the dominant (Ni^{2+}) oxide phase, without contact with the noble metal [37,39]. The Pt $4f_{7/2}$ XPS peak of the bimetallic sample shows two contributions at 70.7 and 72.5 eV, characteristic of the metal (Pd(0)) and oxidized Pt(II) states, respectively.[37,39] The presence of a noble metal oxidized state at the surface of the alloy particles has been previously reported [40]. It is rationalized by the fact that PtNi alloys have a surface layer enriched in Pt with Ni preferentially located at the subsurface layers, altering the response of the monometallic noble metal and facilitating its oxidation [35,41]. It is also noted that the Pt(0) contribution suffers a blue shift with respect to the monometallic Pt reference, indicating that the interaction with Ni withdraws electronic charge from the Pt centers of the alloy. This result further confirms that the PtNi/g-CN sample contains PtNi alloy particles. For all samples and according to the XPS and EELS analyses, we can note the absence of P signal(s) associated with potential residual amounts of the sodium hypophosphite used in the synthesis of PtNi nanoparticles.

Finally, XPS was utilized to investigate the valence band of the catalysts. Figure S6 provides evidence of the absence of significant variations in the valence band position of the samples. Together with the band gap energy values collected in Table 2, it shows that the valence and conduction bands of the semiconductor do not show differences through the catalysts here studied. In particular, absence of significant alternation concerning (conduction and valence) band-edge positions for the metal-containing samples with respect to the bare CN material can be noticed.

3.2. *Catalytic activity and interpretation*

The activity of the samples for the production of hydrogen under illumination is presented in Fig. 5 for the optimum 30:70 methanol to water mixture. Fig. 5A shows that the solids are not active in the absence of light. The bare support as well as the Ni/g-CN sample display rather low activity. The activity of the PtNi/g-CN sample outperforms all systems and particularly the reasonable active monometallic Pt/g-CN sample. The PtNi bimetallic sample also shows a rather good

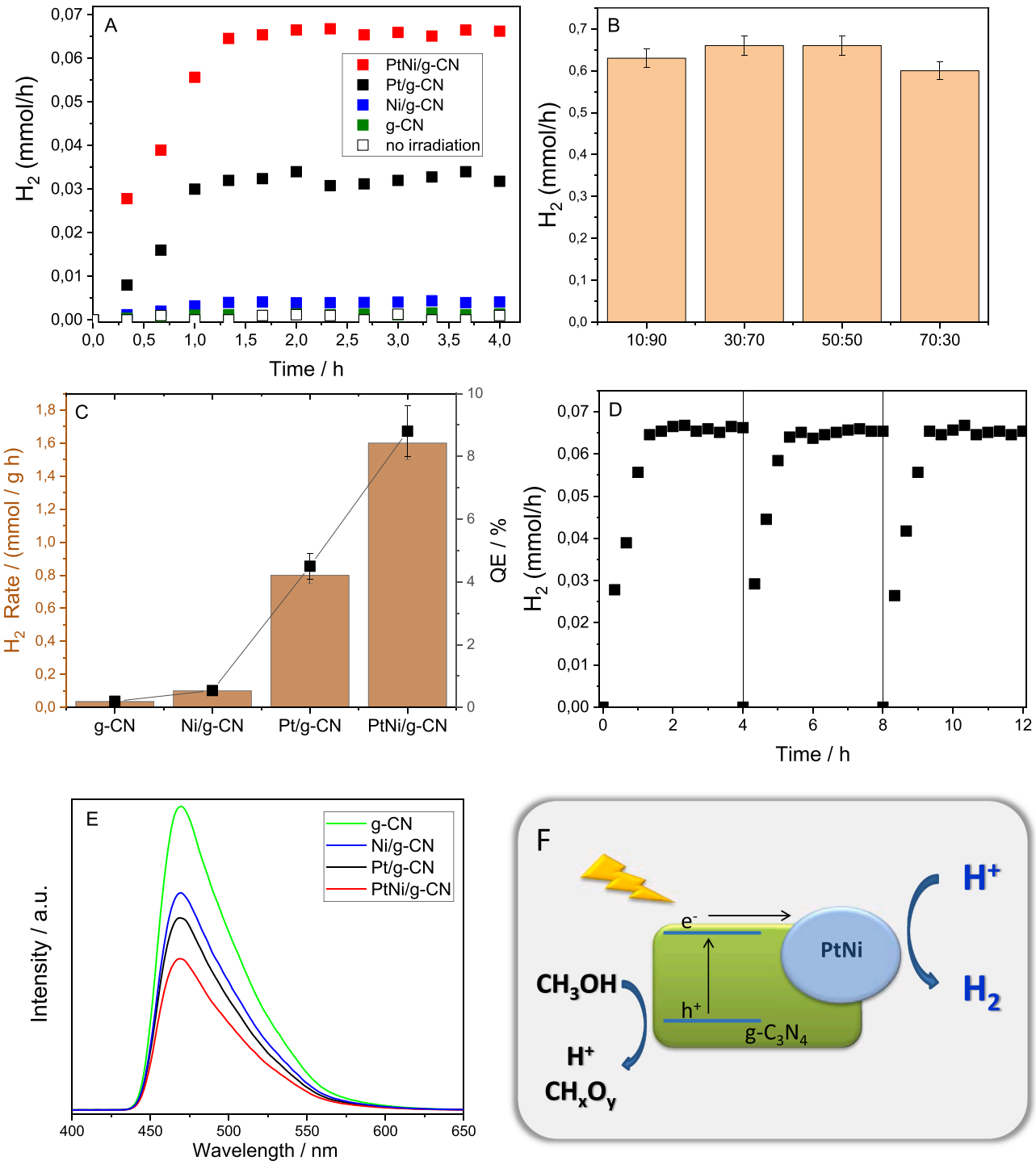

Fig. 5. (A) H_2 production evolution vs. time for the samples. (B) Stationary hydrogen production obtained for the PtNi/g-CN sample vs. the methanol to water content of the liquid phase. (C) Stationary reaction rate and quantum efficiency (QE). (D) H_2 production vs. time for the PtNi/g-CN sample under three consecutive cycles. (E) Photoluminescence spectra for the samples. (F) Esquematic representation of the charge excitation and handling and main steps of the photo-catalytic process.

performance as a function of the methanol-to-water ratio of the liquid phase, although a slight decay of activity is observed for methanol rich cases (Fig. 5B). Activity is here quantified for all samples using the reaction rate and the quantum efficiency (Fig. 5C). The latter is the parameter recommended by the IUPAC to provide a quantitative assessment of the activity [26]. This comes out from the fact that quantum efficiency describes the performance of the catalyst per unit photon (Einstein) absorbed by the powder at reaction conditions. Thus, it provides a measurement of the photo-chemical properties of the corresponding solid surfaces independently of the light absorption capability of the powders [26,27]. The analysis of the quantum efficiency renders values of 0.19 %, 0.53 %, 4.5 % and 8.8 % for the CN, Ni/g-CN, Pt/g-CN and PtNi/g-CN samples, respectively. As already mentioned, the quantum efficiency provides definite proof that bare g-CN support as well as the Ni/g-CN sample show limited performance in the reaction. Pt-containing samples are able to increase the catalytic performance by

one order of magnitude with respect to the mentioned CN and Ni/g-CN powders. This is an expected result. More importantly, the binary PtNi co-catalyst is able to increase the result of the monometallic Pt/g-CN sample by a factor of 1.95. This occurs in spite of the lower content of the noble metal since the bimetallic sample uses roughly half of the Pt content. To the best of our knowledge, the PtNi/g-CN quantum efficiency here measured is the top one among the previously reported studies using Pt and PtNi co-catalysts supported on carbon nitride forms (nanosheets, nanotubes and others) [18,19,42–47]. We remark that our study was carried out using renewable methanol and not using other reagents like TEOA. Using a non-renewable and expensive sacrificial molecule, in these works the reported quantum efficiency goes from ca. 2.0–7.3 % [43–46]. As mentioned, our bimetallic system boosts the activity of the (reasonably active, 4.5 % quantum efficiency) Pt/g-CN sample and reaches a quantum efficiency of 8.8 % (Fig. 5C).

Interestingly, the PtNi/g-CN sample also shows stable behavior under cycling conditions. Fig. 5D presents results for three consecutive cycles of reaction. Note that the stable rate indicates the continuous production of hydrogen in our reactor (hydrogen is constantly removed from the reactor), without important changes after the initial building-up period of each cycle. Therefore, the bimetallic sample does not display any sign of deactivation, confirming the goodness of the catalytic formulation for the photo-production of hydrogen. The inclusion of a binary co-catalyst in a carbon nitride-based formulation renders an active and stable photo-catalyst.

The physico-chemical state of the solids after the reaction was investigated using a multi-technique approach. According to the surface area results, the morphology of the catalysts as well as the main physico-chemical characteristics of the carbon nitride phase are not altered (Table 1). Moreover, the UV–visible spectra and the analysis of the valence band position and band gap energy indicate that neither the optical properties of the solids suffer significant changes (Fig. 1D, S1, and Table 2). The behavior of the co-catalyst was also investigated by testing the XPS spectra after the reaction. First to note is that the metal to (C+N) atomic ratios are not significantly altered for the PtNi/g-CN sample if comparing data before/after the reaction. This powder presents values of $2.5/2.6 \times 10^{-3}$ mol. % in the case of Pt and $7.0/7.0 \times 10^{-3}$ mol% in the case of Ni. Absence of the metals in the liquid phase after the reaction was demonstrated by ICP-AES. Thus, together, these two tests prove that the leaching of the metals during the reaction can be excluded. Second, the Ni oxidation state is essentially not changing in both the Ni/g-CN and PtNi/g-CN samples (Fig. 4 and S4). As mentioned, the rather close behavior of the majority of Ni in these two catalysts can be rationalized by the fact that the majority of Ni in the bimetallic samples is not influenced by the noble metal presence. The monometallic Pt sample also provides a Pt 4f peak without significant changes between the pre and post-reaction specimens (Figure S5). A similar situation takes place with the binary PtNi co-catalyst. The XRD pattern does not show any significant difference (Figure S7). This indicates that the average chemical composition of the PtNi alloy co-catalyst as well as the average particle size of the particles are not altered under reaction conditions. However, a rather modest surface alteration could be detected using XPS. This modification decreases modestly the Pt(0) metal contribution, located at the core of the co-catalyst entities. However, this variation modified the Pt(0)/Pt(II) ratio at the surface layers by less than 15 %.

To interpret the activity results, we carried out a photoluminescence study of the samples. The photoluminescence spectra of the catalysts are presented in Fig. 5D. For all samples, the spectra display a maximum at ca. 470 nm. The intensity of the signal corresponds to band-to-band type de-excitation events which mainly results from the $n - \pi^*$ electronic transitions involving lone pairs of nitrogen atoms in carbon nitride [48]. The intensity of the signal is a measure of the capability of the powder(s) to control the charge carrier recombination phenomenon. A lower intensity would correspond to an improved charge handling capability through the decrease of the recombination and the increasing lifetime of the charge carrier species [6,18]. The comparison with the activity results (Fig. 5C) indicates a key effect of the co-catalyst in all samples. The co-catalyst is able to capture electrons, favoring the separation of charge and increasing the charge carrier lifetime and probability to be involved in chemical steps leading to hydrogen generation [13,14]. Using photoluminescence, it becomes evident the strong correlation between the activity of all samples (Fig. 5C) and the control of the charge carrier recombination phenomenon (Fig. 5E). Therefore, the mentioned correlation demonstrates the critical contribution of the co-catalyst to the control of the photoactivity and explains the activity behavior through the samples of the series. Such a contribution is schematically summarized in Fig. 5F. After excitation with light, which separates charge at the carbon nitride main component, holes located at the valence band will attack the sacrificial molecule generating hydrogen ions. At the same time, electrons promoted to the conduction band of the support will be captured by the PtNi particles and will trigger the coupling of such hydrogen ions to generate the hydrogen molecule, which immediately desorbs and reaches the gas phase, allowing the continuous and stable production of the energy vector.

4. Conclusions

In this work, we studied the use of a binary PtNi co-catalyst deposited using careful synthetic colloidal procedures over a high surface area graphitic type carbon nitride nanosheet type support. In the resulting PtNi/g-CN sample, we observed that the noble metal is part of a Pt-rich alloy (averaged composition ca. 85 % Pt, 15 % Ni) with a surface layer where the noble metal dominates and becomes oxidized as an effect of the presence of the heterometallic bond. Such as oxidation does not occur in the case of the parent single-metal Pt system. The PtNi entities show a rather small primary particle size, about ca. 5 nm, with some particles connected in agglomerates of ca. 10–15 nm. The metals do not suffer any leaching process and are rather stable under reaction conditions, with an absence of particle growth and/or significant changes in the overall chemical composition. The binary PtNi material was tested in the photo-production of hydrogen from methanol:water mixtures. The PtNi/g-CN system provides high and stable activity under cycling conditions. Moreover, it renders a true quantum efficiency of 8.8 % for the photo-production of hydrogen. To our knowledge, this value is the top one among Pt-promoted carbon nitride-based catalysts. Specifically, when compared with a similar Pt/g-CN system, we observed a ca. 2.0 factor for the activity enhancement measured using the quantum efficiency parameter. The excellent performance is a direct consequence of the effect of the presence of PtNi-alloy nanoparticles and the effect of them on the handling of charge carriers produced under illumination, with a significant decrease in the charge carrier recombination and enhancement of the functional properties of the solid.

CRediT authorship contribution statement

Rocío Sayago-Carro: Data curation, Formal analysis, Investigation, Visualization, Writing – review & editing. **Pablo Piqueras-Pérez:** Data curation, Formal analysis, Investigation, Visualization. **Ruifeng Du:** Data curation, Formal analysis, Investigation, Visualization. **Junshan Li:** Data curation, Formal analysis, Investigation, Visualization. **Jing Yu:** Data curation, Formal analysis, Investigation, Visualization. **Jordi Arbiol:** Data curation, Formal analysis, Investigation, Visualization, Writing – review & editing. **Anna Kubacka:** Conceptualization, Data curation, Formal analysis, Funding acquisition, Investigation, Methodology, Project administration, Resources, Software, Supervision, Validation, Visualization, Writing – original draft, Writing – review & editing. **Andreu Cabot:** Conceptualization, Data curation, Formal analysis, Funding acquisition, Investigation, Methodology, Project administration, Resources, Software, Supervision, Validation, Visualization, Writing – original draft, Writing – review & editing. **Marcos Fernández-García:** Conceptualization, Data curation, Formal analysis,

Funding acquisition, Investigation, Methodology, Project administration, Resources, Software, Supervision, Validation, Visualization, Writing – original draft, Writing – review & editing.

Declaration of Competing Interest

The authors declare no conflict of interest.

Data Availability

Data will be made available on request.

Acknowledgments

The authors would like to thank financial support by rants PID2019-105490RB-C31 and PID2019-105490RB-C32 funded by MCIN/AEI/10.13039/501100011033 (Spain) and, as appropriate, by "ERDF A way of making Europe", by the "European Union". M.F.G. is fully indebted to Prof. F. Fernández-Martín for general discussions.

Appendix A. Supporting information

Supplementary data associated with this article can be found in the online version at doi:10.1016/j.jece.2023.110921.

References

[1] M. Ismael, A review and recent advances in solar-to-hydrogen energy conversion based on photocatalytic water splitting over doped-TiO2 nanoparticles, Sol. Energy 211 (2020) 522–546, https://doi.org/10.1016/j.solener.2020.09.073.
[2] Y. Zhao, Y. Li, L. Sun, Recent advances in photocatalytic decomposition of water and pollutants for sustainable application, Chemosphere 276 (2021), 130201, https://doi.org/10.1016/j.chemosphere.2021.130201.
[3] L.V. Mattos, G. Jacobs, B.H. Davis, F.B. Noronha, Production of hydrogen from ethanol: review of reaction mechanism and catalyst deactivation, Chem. Rev. 112 (2012) 4094–4123.
[4] A. Kubacka, M. Fernández-García, G. Colón, Advanced nanoarchitectures for solar photocatalytic applications, Chem. Rev. 112 (2012) 1555–1614, https://doi.org/10.1021/cr100454n.
[5] L. Chang, S.-T. Yong, S.-P. Chai, L.K. Putri, L.-L. Tan, A.R. Mohamed, A review of methanol photoreforming: elucidating the mechanisms, photocatalysts and recent advancement strategies, Mater. Today Chem. 27 (2023), 101334, https://doi.org/10.1016/j.mtchem.2022.101334.
[6] W.-J. Ong, L.-L. Tan, Y.H. Ng, S.-T. Yong, S.-P. Chai, Graphitic carbon nitride (g-C3N4)-based photocatalysts for artificial photosynthesis and environmental remediation: are we a step closer to achieving sustainability? Chem. Rev. 116 (2016) 7159–7329.
[7] G. Marcì, E.I. García-López, L. Palmisano, Polymeric carbon nitride (C3N4) as heterogeneous photocatalyst for selective oxidation of alcohols to aldehydes, Catal. Today 315 (2018) 126–137, https://doi.org/10.1016/j.cattod.2018.03.038.
[8] A. Hayat, A.G. Al-Sehemi, K.S. El-Nasser, T.A. Taha, A.A. Al-Ghamdi, Jawad Ali Shah Syed, M.A. Amin, T. Ali, T. Bashir, A. Palamanit, J. Khan, W.I. Nawawi, Graphitic carbon nitride (g–C3N4)–based semiconductor as a beneficial candidate in photocatalysis diversity, Int. J. Hydrog. Energy 47 (2022) 5142–5191, https://doi.org/10.1016/j.ijhydene.2021.11.133.
[9] T. Ioannidou, M. Anagnostopoulou, K. Christoforidis, Two-dimensional photocatalysts for energy and environmental applications, Solar 2 (2022) 305–320, https://doi.org/10.3390/solar2020017.
[10] N.S.N. Hasnan, M.A. Mohamed, Z.A. Mohd Hir, Surface physicochemistry modification and structural nanoarchitectures of g-C3N4 for wastewater remediation and solar fuel generation, Adv. Mater. Technol. 7 (2022) 2100993, https://doi.org/10.1002/admt.202100993.
[11] A. López-Martín, F. Platero, A. Caballero, G. Colón, Thermo-photocatalytic methanol reforming for hydrogen production over a CuPd−TiO2 catalyst, ChemPhotoChem 4 (2020) 630–637, https://doi.org/10.1002/cptc.202000010.
[12] A. Meng, L. Zhang, B. Cheng, J. Yu, Dual cocatalysts in TiO2 photocatalysis, Adv. Mater. (2019) 1807660, https://doi.org/10.1002/adma.201807660.
[13] C. Xia, T. Hong Chuong Nguyen, X. Cuong Nguyen, S. Young Kim, D.L.T. Nguyen, P. Raizada, P. Singh, V.-H. Nguyen, C. Chien Nguyen, V. Chinh Hoang, Q. Van Le, Emerging cocatalysts in TiO2-based photocatalysts for light-driven catalytic hydrogen evolution: Progress and perspectives, Fuel 307 (2022), 121745, https://doi.org/10.1016/j.fuel.2021.121745.
[14] C.M. Pelicano, M. Saruyama, R. Takahata, R. Sato, Y. Kitahama, H. Matsuzaki, T. Yamada, T. Hisatomi, K. Domen, T. Teranishi, Bimetallic synergy in ultrafine cocatalyst alloy nanoparticles for efficient photocatalytic water splitting, Adv. Funct. Mater. 32 (2022) 2202987, https://doi.org/10.1002/adfm.202202987.
[15] P. Jimenéz-Calvo, M.J. Muñoz-Batista, M. Isaacs, V. Ramnarain, D. Ihiawakrim, X. Li, M. Ángel Muñoz-Márquez, G. Teobaldi, M. Kociak, E. Paineau, A compact photoreactor for automated H2 photoproduction: revisiting the (Pd, Pt, Au)/TiO2 (P25) Schottky junctions, Chem. Eng. J. 459 (2023), 141514, https://doi.org/10.1016/j.cej.2023.141514.
[16] U. Caudillo-Flores, M.J. Muñoz-Batista, A. Kubacka, M. Fernández-García, Pd-Pt bimetallic Nb-doped TiO2 for H2 photo-production: gas and liquid phase processes, Mol. Catal. 481 (2020), 110240, https://doi.org/10.1016/j.mcat.2018.11.011.
[17] U. Caudillo-Flores, I. Barba-Nieto, M.N. Gómez-Cerezo, A. Martinez-Arias, M. Fernandez-Garcia, A. Kubacka, Towards the green production of H2: binary Pt-Ru promoted Nb-TiO2 based photo-catalysts, ACS Sustain. Chem. Eng. 7 (2019) 15671–15683.
[18] L. Bi, X. Gao, Z. Ma, L. Zhang, D. Wang, T. Xie, Enhanced separation efficiency of PtNi x/g-C3N4 for photocatalytic hydrogen production, ChemCatChem 9 (2017) 3779–3785, https://doi.org/10.1002/cctc.201700640.
[19] P. Wang, L. Zong, Z. Guan, Q. Li, J. Yang, PtNi alloy cocatalyst modification of eosin Y-Sensitized g-C3N4/GO hybrid for efficient visible-light photocatalytic hydrogen evolution, Nanoscale Res. Lett. 13 (2018) 33, https://doi.org/10.1186/s11671-018-2448-y.
[20] G.K. Williamson, W.H. Hall, X-ray line broadening from filed aluminium and wolfram, Acta Met. 1 (1953) 22–31, https://doi.org/10.1016/0001-6160(53)90006-6.
[21] P. Kubelka, New contributions to the optics of intensely light-scattering materials. Part I, J. Opt. Soc. Am. 38 (1948) 448–457, https://doi.org/10.1364/JOSA.38.000448.
[22] G. Dong, Y. Zhang, Q. Pan, J. Qiu, A fantastic graphitic carbon nitride (g-C3N4) material: Electronic structure, photocatalytic and photoelectronic properties, J. Photochem. Photobiol. C Photochem. Rev. 20 (2014) 33–50, https://doi.org/10.1016/j.jphotochemrev.2014.04.002.
[23] D.A. Shirley, High-resolution X-ray photoemission spectrum of the valence bands of gold, Phys. Rev. B 5 (1972) 4709–4714, https://doi.org/10.1103/PhysRevB.5.4709.
[24] O. Fontelles-Carceller, M.J. Muñoz-Batista, E. Rodríguez-Castellón, J.C. Conesa, M. Fernández-García, A. Kubacka, Measuring and interpreting quantum efficiency for hydrogen photo-production using Pt-titania catalysts, J. Catal. 347 (2017) 157–169, https://doi.org/10.1016/j.jcat.2017.01.012.
[25] U. Caudillo-Flores, M.J. Muñoz-Batista, M. Fernández-García, A. Kubacka, Bimetallic Pt-Pd co-catalyst Nb-doped TiO2 materials for H2 photo-production under UV and Visible light illumination, Appl. Catal. B Environ. 238 (2018) 533–545, https://doi.org/10.1016/j.apcatb.2018.07.047.
[26] S.E. Braslavsky, A.M. Braun, A.E. Cassano, A.V. Emeline, M.I. Litter, L. Palmisano, V.N. Parmon, N. Serpone, Glossary of terms used in photocatalysis and radiation catalysis (IUPAC recommendations 2011), Pure Appl. Chem. 83 (2011) 931–1014, https://doi.org/10.1351/PAC-REC-09-09-36.
[27] U. Caudillo-Flores, M.J. Muñoz-Batista, M. Fernández-García, A. Kubacka, Recent progress in the quantitative assessment and interpretation of photoactivity, Catal. Rev. (2023), https://doi.org/10.1080/01614940.2022.2075535 (in press).
[28] M.J. Muñoz-Batista, O. Fontelles-Carceller, A. Kubacka, M. Fernández-García, Effect of exfoliation and surface deposition of MnOx species in g-C3N4: toluene photo-degradation under UV and visible light, Appl. Catal. B Environ. 203 (2017) 663–672, https://doi.org/10.1016/j.apcatb.2016.10.044.
[29] R. Du, K. Xiao, B. Li, X. Han, C. Zhang, X. Wang, Y. Zuo, P. Guardia, J. Li, J. Chen, J. Arbiol, A. Cabot, Controlled oxygen doping in highly dispersed Ni-loaded g-C3N4 nanotubes for efficient photocatalytic H2O2 production, Chem. Eng. J. 441 (2022), 135999, https://doi.org/10.1016/j.cej.2022.135999.
[30] S. Lee, H.J. Kim, S.M. Choi, M.H. Seo, W.B. Kim, The promotional effect of Ni on bimetallic PtNi/C catalysts for glycerol electrooxidation, Appl. Catal. A Gen. 429–430 (2012) 39–47, https://doi.org/10.1016/j.apcata.2012.04.002.
[31] W. Yu, M.D. Porosoff, J.G. Chen, Review of Pt-based bimetallic catalysis: from model surfaces to supported catalysts, Chem. Rev. 112 (2012) 5780–5817, https://doi.org/10.1021/cr300096b.
[32] L. Dubau, J. Nelayah, S. Moldovan, O. Ersen, P. Bordet, J. Drnec, T. Asset, R. Chattot, F. Maillard, Defects do catalysis: CO monolayer oxidation and oxygen reduction reaction on hollow PtNi/C nanoparticles, ACS Catal. 6 (2016) 4673–4684, https://doi.org/10.1021/acscatal.6b01106.
[33] E. Zen, Validity of "vegard's law, Am. Mineral. 41 (1956) 523–524.
[34] L. Vegard, Die Konstitution der Mischkristalle und die Raumfüllung der Atome, Zeitschrift Für Phys 5 (1921) 17–26, https://doi.org/10.1007/BF01349680.
[35] G. WANG, M. VANHOVE, P. ROSS, M. BASKES, Quantitative prediction of surface segregation in bimetallic Pt–M alloy nanoparticles (M=Ni,Re,Mo, Prog. Surf. Sci. (2005), https://doi.org/10.1016/j.progsurf.2005.09.003.
[36] R.M. Arán-Ais, F. Dionigi, T. Merzdorf, M. Gocyla, M. Heggen, R.E. Dunin-Borkowski, M. Gliech, J. Solla-Gullón, E. Herrero, J.M. Feliu, P. Strasser, Elemental anisotropic growth and atomic-scale structure of shape-controlled octahedral Pt–Ni–Co alloy nanocatalysts, Nano Lett. 15 (2015) 7473–7480, https://doi.org/10.1021/acs.nanolett.5b03057.
[37] C.D. Wagner, G.E. Muilenberg, Handbook of X-ray Photoelectron Spectroscopy: A Reference Book of Standard Data for Use in X-ray Photoelectron Spectroscopy, Perkin-Elmer, 1979.
[38] A.S. Karakoti, J.E.S. King, A. Vincent, S. Seal, Synthesis dependent core level binding energy shift in the oxidation state of platinum coated on ceria–titania and its effect on catalytic decomposition of methanol, Appl. Catal. A Gen. 388 (2010) 262–271, https://doi.org/10.1016/j.apcata.2010.08.060.
[39] X. Xie, A.L.M. Sandhya, L. Piliai, M. Vorokhta, I. Matolínová, I. Khalakhan, Surface compositional dynamics in a PtNi bimetallic alloy under simulated operational conditions: Electrochemical and NAP-XPS Study, Appl. Catal. B Environ. 325 (2023), 122328, https://doi.org/10.1016/j.apcatb.2022.122328.

[40] I. Khalakhan, L. Vega, M. Vorokhta, T. Skála, F. Viñes, Y.V. Yakovlev, K. M. Neyman, I. Matolínová, Irreversible structural dynamics on the surface of bimetallic PtNi alloy catalyst under alternating oxidizing and reducing environments, Appl. Catal. B Environ. 264 (2020), 118476, https://doi.org/10.1016/j.apcatb.2019.118476.

[41] G. Wang, M.A. Van Hove, P.N. Ross, M.I. Baskes, Monte Carlo simulations of segregation in Pt-Ni catalyst nanoparticles, J. Chem. Phys. 122 (2005), 024706, https://doi.org/10.1063/1.1828033.

[42] M.J. Muñoz-Batista, D. Rodríguez-Padrón, A.R. Puente-Santiago, A. Kubacka, R. Luque, M. Fernández-García, Sunlight-driven hydrogen production using an annular flow photoreactor and g-C3N4-based catalysts, ChemPhotoChem 2 (2018) 870–877, https://doi.org/10.1002/cptc.201800064.

[43] H. Zhao, S. Wang, F. He, J. Zhang, L. Chen, P. Dong, Z. Tai, Y. Wang, H. Gao, C. Zhao, Hydroxylated carbon nanotube/carbon nitride nanobelt composites with enhanced photooxidation and H2 evolution efficiency, Carbon N. Y 150 (2019) 340–348, https://doi.org/10.1016/j.carbon.2019.05.020.

[44] L. Bi, R. Zhang, K. Zhang, Y. Lin, D. Wang, X. Zou, T. Xie, Sulfidization of platinum nickel bimetal-decorated g-C 3 N 4 for photocatalytic hydrogen production: photogenerated charge behavior study, ACS Sustain. Chem. Eng. 7 (2019) 15137–15145, https://doi.org/10.1021/acssuschemeng.9b04153.

[45] S. Sun, Y. Feng, L. Pan, X. Zhang, J.-J. Zou, Integrating Pt@Ni(OH) nanowire and Pt nanoparticle on C N4with fast surface kinetics and charge transfer towards highly efficient photocatalytic water splitting, Appl. Catal. B Environ. 259 (2019), 118028, https://doi.org/10.1016/j.apcatb.2019.118028.

[46] H. Bao, L. Wang, G. Li, L. Zhou, Y. Xu, Z. Liu, M. Wu, Carrier engineering of carbon nitride boosts visible-light photocatalytic hydrogen evolution, Carbon N. Y 179 (2021) 80–88, https://doi.org/10.1016/j.carbon.2021.04.018.

[47] S. Zhao, C. Zhang, Y. Wang, K. Zhao, Y. Zhou, L. Li, S. Zhuo, Facile construction of carbon doped carbon nitride tube with increased π-electron density for highly efficient hydrogen production, Colloids Surf. A Physicochem. Eng. Asp. 660 (2023), 130872, https://doi.org/10.1016/j.colsurfa.2022.130872.

[48] Q. Xiang, J. Yu, M. Jaroniec, Preparation and enhanced visible-light photocatalytic H 2 -production activity of graphene/C 3N4 composites, J. Phys. Chem. C. 115 (2011) 7355–7363, https://doi.org/10.1021/jp200953k.